PHYSICAL REVIEW E **100**, 013106 (2019)

Experimental characterization of the growth dynamics during capillarity-driven droplet generation

Bhaskarjyoti Sarma, Vijay Shahapure, Amaresh Dalal,[*] and Dipankar N. Basu[†]
Department of Mechanical Engineering, Indian Institute of Technology Guwahati, Guwahati-781039, India

(Received 14 March 2019; revised manuscript received 30 May 2019; published 15 July 2019)

The transient dynamics of a growing droplet in a yarn is explored following the spatiotemporal evolution of the three-phase contact line as well as the liquid-air interface with the help of videographic techniques and subsequent image analyses. The spontaneous capillary flow of liquids in a porous network is used to generate a droplet on the freely hanging end of a yarn whose other end is dipped continuously in a liquid reservoir. The growing droplet initially moves upward due to surface tension until the attainment of a critical volume, beyond which gravity is able to pull it downward until detachment. Based upon the spatiotemporal trajectory of the three-phase contact line of the droplet, the entirety of the associated growth dynamics can be divided in three distinct regimes, namely, "radial growth," "axial growth," and "motion" stages. The transition from one to the other is governed by the subtle interplay between the capillary and the gravity forces. Several experimental fluids are considered to elucidate the effect of the fluid properties on the transient contact line and interfacial dynamics of drops. The kinetics of the three-phase contact line and the radius of the droplet is found to follow two distinct exponential scaling laws, developed through the combination of the relevant forces. A mathematical model has also been proposed to predict the critical volume of the growing droplet in relation to its final volume, beyond which gravity controls the transient dynamics.

DOI: 10.1103/PhysRevE.100.013106

I. INTRODUCTION

The transmission of liquids through the porous network of the naturally abundant, as well as the synthetic objects, is a ubiquitous phenomenon and has been studied extensively both by the researchers and industrialists since ages [1–7]. Specifically, the immense potential of spontaneous capillary flows (SCF) in transporting liquids through the porous networks of yarns, without the use of external pumping, have been put into use in numerous industrial and day-to-day applications which primarily encompass textile [8,9], mold preparation industries [10], biomedical devices [11–13], forensic laboratories [14,15], household drying [16,17], coating processes, etc. The wicking ability of the constituent yarns emerges to be one of the most influential parameters for successful operation of these devices and processes, as has been envisaged in several experimental and analytical studies [3,18–22].

Drop formation from a nozzle or orifice is another interesting hydrodynamic phenomenon with a wide and varied range of uses, such as inkjet printing [23,24], spray formation [25,26], DNA microarray deposition [27], microencapsulation [28,29], etc. The rich underlying physics associated with the dynamics of growth and breakup of a liquid drop from a nozzle (or orifice) has been explored exhaustively with the help of experimental [30–33] and computational techniques [34–38] over the last few decades. Two contrasting modes of drop formation dynamics, namely, dripping and jetting [33,39], have been identified with the help of high-speed visualization techniques and subsequent image processing [40,41]. One of the pioneering attempts to capture the bifurcation process of pendant drops was reported by Hauser *et al.* [42] and was reproduced a decade later by Peregrine *et al.* [43]. In recent years, owing to the advancement of high-speed imaging techniques, researchers are able to visibly explore many intricate physics of drop formation and breakup, the crucial dynamics in the vicinity of pinch-off [37,44] in particular, which remained unfathomed only until the last decade. Such advanced experimental tools and methods have immense contributions in uncovering the relevant phenomenon, leading to some wonderful recent efforts, such as the formation of a drop from a wettable nozzle [45], tilted nozzle [46], droplet formation in dense suspension [47], etc., which has high relevancy with the industrial processes.

Therefore, it is very much evident that numerous research works have separately explored drop formation in nozzles and wicking in yarns. However, we have not found any effort toward integrating both in the form of drop generation by wicking in the porous network of a yarn. This study makes an honest attempt to bridge this gap by unveiling the dynamics of drop formation from an unwoven yarn under varying flow conditions. A simple experimental arrangement constructed by using a yarn, as shown in Fig. 1, serves the purpose of addressing many new aspects in the regime of drop dripping, that have heretofore been unexplored. The prime focus of this paper is a systematic investigation of the transient dynamics of the three-phase (air-liquid-yarn) contact line of the droplet during its growth in a yarn under the effect of gravity and interfacial forces. By bringing the yarn in contact with the liquid in a reservoir, a flow field can be established owing to the continuous wicking of the liquid in

---

[*] Corresponding author: amaresh@iitg.ac.in
[†] Corresponding author: dnbasu@iitg.ac.in

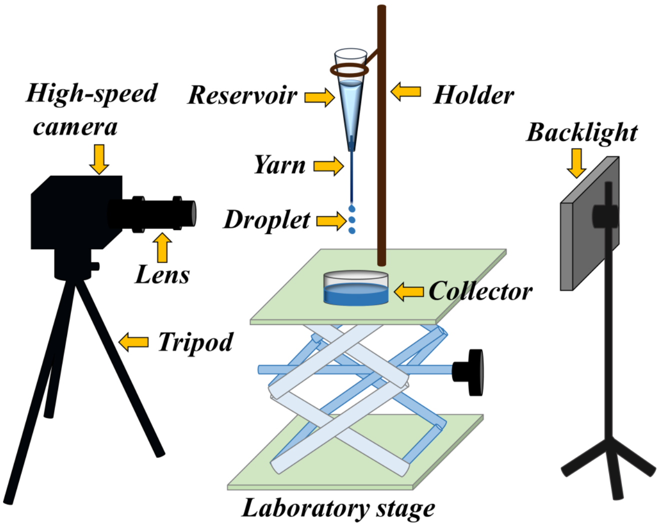

FIG. 1. Schematic diagram of the experimental setup with all the components.

the available porous network. Once the yarn is saturated, the continuously incoming liquid generates a bulb of liquid mass at the freely hanging end, which develops in volume with time. The contact line of the droplet with the yarn has distinct vertical motion during the complete growth period, which can subsequently be classified into multiple regimes. With the help of videographic techniques and image analyses, we try to capture the transient dynamics in each of these regimes, followed by the consequent data analysis to achieve a unified description of the underlying physical phenomena in terms of the competing forces controlling the dynamics of the contact line movement. This kind of distinct vertical motion of the contact line is ubiquitously seen during the capillary rise of a liquid in a wettable tube [48] or porous material [49] or droplet sliding along a wettable surface [50] as well as in the rare case of drop formation in a wettable nozzle [45], while being a rarity during the drop generation from nonwettable nozzles [30,51,52].

The organization of the rest of the study is as follows. The experimental procedures and materials have been discussed in Sec. II, while the results and discussions are presented in Sec. III. The concluding remarks are drawn in Sec. IV.

II. EXPERIMENTAL METHOD AND MATERIALS

Figure 1 shows the schematic of the experimental setup developed for this study, which involves a yarn hanging from an infinite liquid reservoir. A filament type yarn with an average diameter in the range of 1.5 ± 0.08 mm in the as-procured condition plays the role of the droplet generator, and a microtip of 1000 microliter volume behaves as the infinite fluid reservoir, constantly supplying the fluid necessary for drop formation. The yarn consists of 4 fibers or filaments, having an average diameter in the range of 0.86 ± 0.03 mm. All the yarns are cut out at a length of 40 mm from a large roll of the same and checked for length and diameters by using an optical microscope (Leica DM 2500M) before using in the experiments. For each set of experimental conditions, a separate pair of reservoir and yarn has been used. The liquid level at the reservoir has been kept constant for each experimental cycle to nullify the effect of variation in the hydrostatic pressure on the capillary flow rate. Special attention has also been given while placing the yarn in contact with the reservoir, to ensure that the capillary penetration takes place only due to the transplanar wicking mode, while the rest of the wicking modes remain suppressed [19]. Moreover, a simple knot has been provided in the yarn at the end dipped in the liquid reservoir in order to prohibit any sidewise leakage and to obtain drop formation only due to capillary flow within the fiber.

TABLE I. Properties of experimental fluids. DIW = DI-water, Gly. = Glycerol, Twn20 = Tween 20.

Liquid	Density (ρ, kg/m^3)	Viscosity (η, mPas)	Surface tension (γ, mN/m)
DIW	1000.0	1.0	72.0
2% Twn20 sol.	1000.34	1.04	36.3
40% DIW + 60% Gly.	1165.4	12.75	69.5
Hexadecane	770.0	3.0	27.0

The experiments have been carried out for four different liquids, namely, DI-water (DIW, Merck Millipore, grade I, resistivity 18.2 MΩ cm at 25 °C), hexadecane (Hexd), 60% glycerol (aqueous) solution (Gly60), and 2% Tween 20 solution in DI-water (Twn20). The relevant thermophysical properties, namely, viscosity, surface tension, and density of each of the experimental fluids have been measured with the help of rheometer (PHYSICA MCR 101; Aanton Paar), tensiometer (DY-300; Kyowa), and density meter (Aanton Paar; DMA 4500), respectively, and are listed in Table I. The working fluids are chosen in such a way that working range of viscosity and surface tension spans across a wide range.

The video recordings of the experiments have been carried out with a digital camera (Cybershot DSC-HX100v, SONY Crop. Japan) at a frame rate of 25 frames per second. A bright LED Light (Phlox, 130000 Lux) placed opposite to the recorder, as shown in Fig. 1, provides continuous backlighting in all the experimental conditions. This arrangement ensures a sharp contrast of the interfaces relative to the background. The recorded images are then stored in a PC for subsequent image processing and analysis. An open source image processing software ImageJ [53] has been used for the analysis of the captured experimental images.

The fluid properties expected to influence the dynamics of drop formation are surface tension (γ), density (ρ), and viscosity (η) of the penetrating fluid, which further can be clubbed together to form the following set of nondimensional numbers: We, Fr, and Oh, pertinent to the physics involved in this study. Here, the Weber number $\mathrm{We} = \rho v_{\mathrm{avg}}^2 L/\gamma$ signifies the relative importance of the inertia force to the capillary force, the Froude number $\mathrm{Fr} = v_{\mathrm{avg}}/\sqrt{gL}$ signifies the relative importance of inertia force to the gravitational force, and the Ohnesorge number $\mathrm{Oh} = \eta/\sqrt{\rho\gamma \mathrm{L}}$ expresses the relative importance of viscous force over the inertial force and capillary force. Herein, the radius of the yarn r_y has been scaled as the characteristic length L and the average flow velocity $v_{\mathrm{avg}}\ (= Q/\pi r_y^2)$ has been scaled as the characteristic velocity while calculating the nondimensional numbers. Q is the

TABLE II. Experimental conditions for this study. DIW = DI-water, Twn20 = Tween 20 (2% solution), Hexd = Hexadecane, Gly60 = 60% Glycerol + 40% DIW.

Flow rate	$Q\times10^{11}(\mathrm{m}^3/\mathrm{s})$	$\mathrm{We}\times10^9$	$\mathrm{Oh}\times10^3$	$\mathrm{Fr}\times10^5$
Q^{DIW}	56.8 ± 5	1078.7 ± 100	4.3	375.10 ± 10
Q^{Twn20}	8.68 ± 0.3	50.31 ± 3	6.33	57.32 ± 5
Q^{Hexd}	2.06 ± 0.2	2.90 ± 0.1	24.1	13.6 ± 2
Q^{Gly60}	0.63 ± 0.07	0.16 ± 0.03	51.7	4.2 ± 0.3

average flow rate of the penetrating fluid through the porous network, measured by volumetric fluid measurement method. Table II lists the values of the nondimensional numbers along with the corresponding flow rates.

III. RESULTS AND DISCUSSION

This section presents a detailed appraisal of the transient dynamics associated with the generation of a droplet from a yarn. The discussion commences by describing the growth history of a water droplet in yarn, subsequently evolving into the exploration of the transient dynamics of the contact line in case of viscous Newtonian droplets. An attempt has further been made for developing a couple of unified scaling laws, describing the contact line motion, and interfacial shape change (specifically radial expansion) for all the experimental conditions considered herein (refer Table II).

In the present experimental conditions, spontaneous capillary flow within the porous network of the yarn engendered the formation of a droplet, which grows in time due to the accumulation of the continuously incoming mass of liquid. This growing fluidic bulb experiences a series of changes in geometry, starting with the barrel shape at the beginning to the pear shape prior to the detachment, alongside the associated contact line movements. The plethora of events, as depicted sequentially in Fig. 2, starts with the growth of the droplet in both radial and axial directions, which is followed by downward motion of the liquid bulb until it reaches the free end of the yarn, where it finally detaches, yielding a parent droplet and a satellite one.

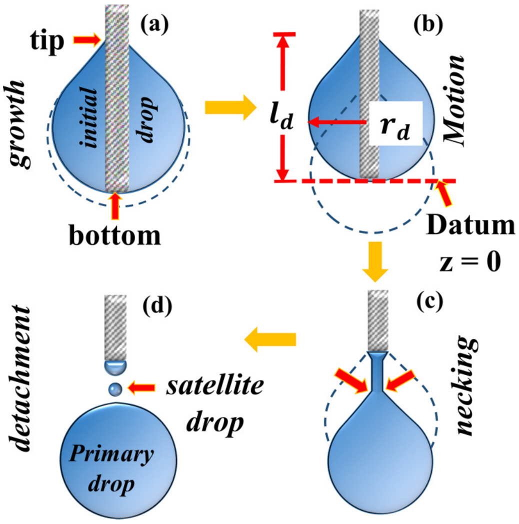

FIG. 2. Schematic diagram of the different stages involved in drop formation from a yarn, namely, (a) growth ("radial" and "axial"), (b) "motion," (c) "necking," and (d) "detachment." The yellow arrows show the sequence of the occurrence of the events. The two red arrows in the image (a) show the position of two points of interest, namely, "tip" and "bottom," referred for describing the growth dynamics of the droplets in yarn. The variables l_d and r_d, shown in image (b) with respective positions of measurements, represent the length and radius of the droplet, respectively. The red dashed line drawn in the free end of the yarn in image (b) represents the position of the datum $z = 0$ considered for various measurements during the study.

In order to elicit and quantify the growth history of the droplet, the present discussion considers the spatiotemporal evolution of the trajectory of two points around the droplet, naming them as "tip" and "bottom" as shown in Fig. 2(a). The "tip," referred as z_{tp}, corresponds to the three-phase contact line (TPCL) of the droplet with the yarn, whereas the bottommost point of the droplet along the yarn has been named as "bottom" (referred as z_{bt}). The relative positioning of these two points from the datum, i.e., $z = 0$, has been used to quantify the movement and location of the droplet along the axial direction of the yarn. It is to note that the free end of the hanging yarn has been considered as the datum [please refer Fig. 2(b)] for the ease of referencing and quantifying the trajectories. The exact location of the "tip" has been identified in a two-step process: first, we convert the raw images into binary images in ImageJ software, which helps in marking of the exact pixels representing the "tip" in the zoomed view of the binary images. Next, we visually track the position of the TPCL indicated by the change or movement in the intensity of the pixels between two consecutive images considered. Similarly, to track the dynamics of the shape change, the maximum radius of the droplet at each instant is found to be of paramount importance and it has been identified schematically in Fig. 2(b) by a variable r_d. Further, the length of the droplet has been deduced as the difference in position between the "tip" and "bottom" at each instance, i.e., $l_d = z_{tp} - z_{bt}$. In what follows, the temporal evolution of the trajectories (z_{tp} and z_{bt}), as well as the droplet radius r_d, have been explored for a wide range of experimental conditions (listed in Table II) to unfurl the transient growth dynamics of the droplet as well as different transitional regimes, as shown in Secs. III A–III E.

A. Growth dynamics of water droplets

Figure 3 (and Supplemental Material, video 1 [54]) shows snapshots of the spatiotemporal evolution of the interface and the contact line of a water droplet during its growth from a yarn. Herein, the instant of detachment of the previous drop has been considered as $t = 0$ in the physical timescale, which acts as a reference for the subsequent snapshots. Also, the position of the "tip" at each instance is marked by the red arrows, a convention followed meticulously in the remainder of the paper. It can be inferred from Figs. 3(a)–3(c) that, at the onset, the contact line of the water drop, i.e., "tip" starts moving upward, along with the continuous radial expansion of the droplet resulting in a growing bulb. The upward movement of the "tip" also results in augmentation in the length of the droplet. Both this radial and axial expansion leads to

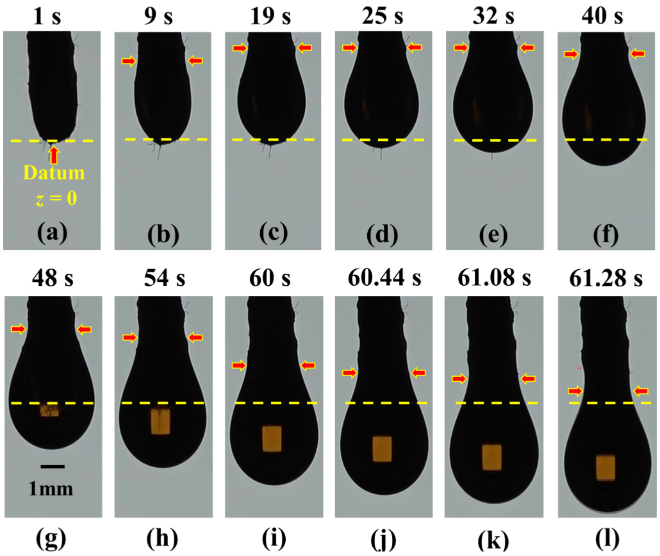

FIG. 3. Spatiotemporal evolution of the droplet interface during the generation of water drop from a yarn. The corresponding experimental conditions are We = 1.078×10^{-6}, Oh = 0.0043, Fr = 3.76×10^{-3}. The red arrows mark the position of the three-phase contact line of the droplet ("tip") at different instances, whereas the yellow dashed lines in the snapshots refer to the location of datum. The scale bar shows 1 mm in length. The events have been recorded at 25 frames per second using a SONY camcorder.

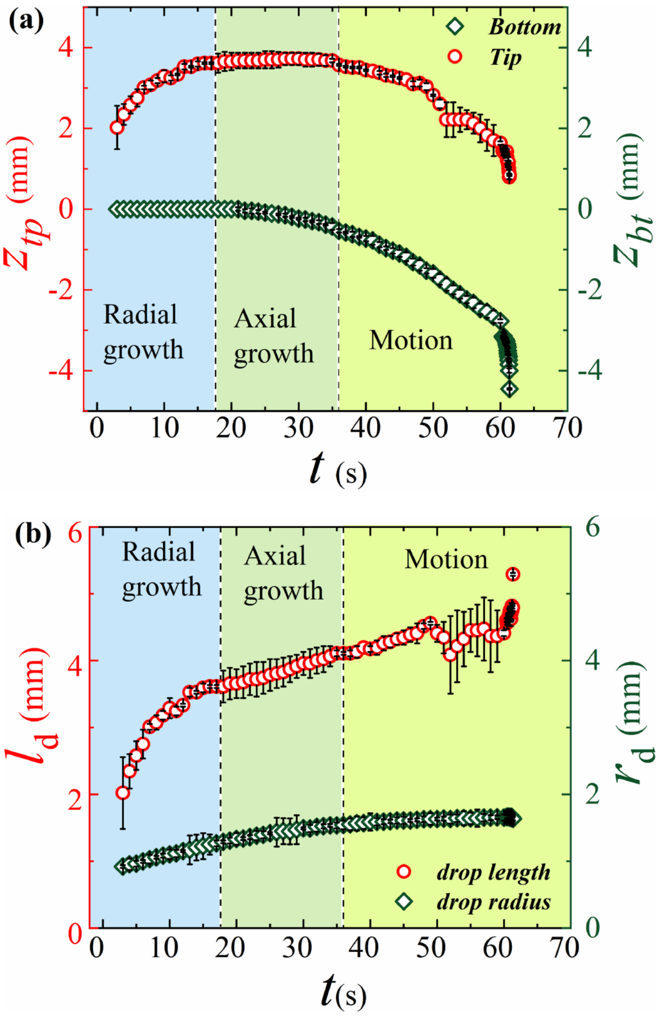

FIG. 4. (a) The temporal variation of the position of tip z_{tp} and bottom z_{bt} points during the growth of a water drop. (b) The variation of length l_d and radius r_d of a water drop during its growth stage. Position of the tip and bottom below the datum, i.e., $z = 0$ (yellow dashed line in Fig. 3) is considered as negative, while the position above it has been considered as positive. The dashed vertical lines delineate the three stages of drop growth in both (a) and (b). The corresponding experimental conditions are We = 1.078×10^{-6}, Oh = 0.0043, Fr = 3.76×10^{-3}. The uncertainties in the measurement of the position of the respective identities at each instant are marked by the error bars associated with each data point.

a consequent increment in the contact angle of the droplet, thereby changing the shape of the droplet from barrel shape at the onset to the pear shape as seen in Fig. 3(c). However, as soon as the value of the contact angle reaches saturation (approximately 10°), the upward movement of the "tip" gets arrested, indicating the beginning of the second phase [refer to Fig. 3(c)]. The delicate balance between the surface energy and the gravitational energy determines this saturation contact angle as well as the shape of the interface at each instance. This first stage of the droplet growth has been coined as "radial growth" stage, owing to the relatively higher rate of radial expansion in comparison to the axial expansion, which shall be discussed elaborately in the subsequent sections.

At the beginning of the second stage, the "tip" starts dwelling at its maximum position, whereas, the "bottom" starts moving away from the datum $z = 0$, as seen in Figs. 3(d) and 3(e), accommodating the continuously incoming mass of liquid. The dynamics results in a significant increase in the total length of the droplet, although the interface of the droplet continues to be pear shaped. This second stage having a higher rate of expansion in the axial direction can be termed as "axial growth" stage. The continuous radial and the axial expansion results in a continuous enhancement in the droplet volume until the moment it attains a critical volume (discussed later on separately in Sec. III D), beyond which the gravitational pull is able to overcome the resisting forces (namely, capillary forces at the contact line). This initiates a sliding motion of the bulbous mass in the downward direction, as seen in Figs. 3(f)–3(l), which persists until the detachment of the droplet from the yarn. Compared to the previous two stages, this stage has a significantly longer time span during the growth of the drop, named as "motion" stage. In one of the following subsections, it will be shown quantitatively that during this stage the change in the droplet volume is minimal, whereas it bears the distinct sign of the movement of the contact line, which again justifies the term coined to this stage.

An account of the temporal variation in the positions of the "tip" (circle) and "bottom" (diamond) helps in capturing the transient dynamics of the contact line, as well as easy delineation of the above mentioned three stages as seen in Fig. 4(a). Each of the three stages is found to have distinct characterizing slopes, with the corresponding points of inflection marking the transition from one stage to the other. With the "tip" climbing upward and the "bottom" of the droplet dwelling at the datum, i.e., $z_{bt} = z = 0$, the accumulated fluid mass expands radially in the first regime, exhibiting

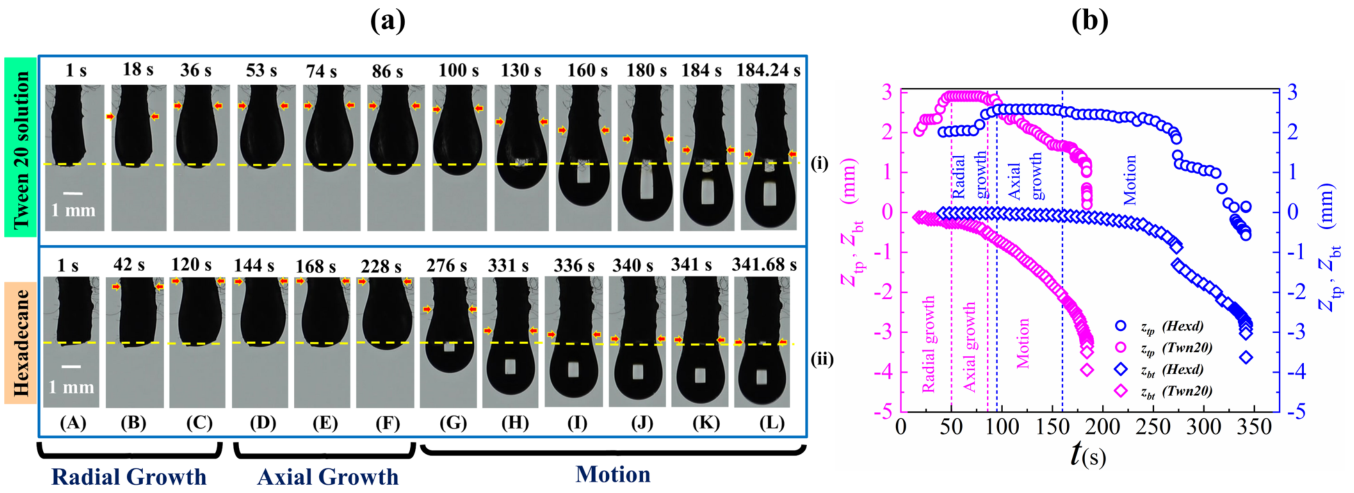

FIG. 5. (a) Spatiotemporal evolution of the interface during the generation of (i) tween 20 and (ii) hexadecane droplet from a yarn. The red arrows mark the position of the three-phase contact line (tip) at different instants. The scale bar shows 1 mm in length. The corresponding experimental conditions are We $= 5.03 \times 10^{-8}$, Oh $= 0.0063$, Fr $= 5.73 \times 10^{-4}$, and We $= 2.90 \times 10^{-9}$, Oh $= 0.024$, Fr $= 1.36 \times 10^{-4}$ for rows (i) and (ii), respectively. The yellow dashed lines in the snapshots of rows (i) and (ii) show the datum. (b) The temporal variation in the position of the tip and bottom during the growth of droplets of tween 20 solution and hexadecane, in a yarn. The data of this plot correspond to the images of Fig. 5(a). The two different colors of the same symbols represent the data corresponding to tip and bottom for the two different experimental liquids. The differently colored dotted vertical lines delineate all the three stages seen during the drop growth period.

a time period of approximately 20 s in all the experiments done with water as the working fluid. As calculated from the experimental data plotted in Fig. 4(a), the contact line achieves a maximum velocity of approximately 0.3 mm/s while climbing upward. Although a sharp change in the slope is present in the trajectory of the tip while it enters the second stage, the transition of the bottom appears to be noticeably smoother [Fig. 4(a)]. The pinning of the tip at its maximum position is the characteristic transient dynamic of this second regime, which seems to have a time period of approximately 15 s. Also, the plot clearly reveals the continuous movement of the bottom, veering away from the datum during this "axial growth" stage. The depinning of the tip happens as soon as the weight of the continuously growing bulb overcomes the resisting forces. In Sec. III D we try to theoretically model this critical volume of the growing droplet through a delicate force balance between the driving and resisting forces. Although the trajectory of the tip further experiences a sudden change in the slope at the beginning of the third stage, however, it moves in a near synchronous manner with the trajectory of the bottom as the dynamics of the third stage evolves. The tip starts sliding toward the datum, i.e., the end of the yarn and the bottom kept on moving away from the yarn end as shown in Fig. 4(a). The differently colored regimes represent the extent of a particular regime, whereas the common boundary marked by the dashed line signifies the borderline of transition between the three different regimes.

Furthermore, for a systematic investigation of the temporal evolution of the interface, we plot the temporal variation of the radius r_d and the length l_d of the droplet in Fig. 4(b). Notably, both the curves clearly hint toward the presence of three distinct regimes of droplet growth. While the different regimes are prominent along the curve of l_d due to the presence of sharp changes in its slope, the curve of r_d has a relatively smoother transition from one regime to the other. Qualitatively, both r_d and l_d increase continuously due to the accumulation of the incoming fluidic mass. However, the rate of radial expansion slows down as the dynamics progresses toward detachment, as reflected from the continually decreasing slope of the r_d curve at each stage. Interestingly, the time period of occurrence and transition of the dynamics of both the movement of the contact line and the interfacial shape change coincides with each other for all the stages during the droplet growth as seen Figs. 4(a) and 4(b). This mutual dependence between the contact line movement and shape change dynamics has further been extended for the growth of more viscous liquids (than water) in the following subsection.

B. Effect of enhanced viscosity of the penetrating fluid

This section explores the effect of an increase in viscosity of the penetrating fluid on the dynamics of growth of a droplet from a yarn. Increase in viscosity is achieved by allowing capillary penetration of different experimental fluids, as listed in Table I, with viscosity ranging from 1.04 to 12.75 mPas. As confirmed by Washburn's law of wicking [1,55] as well as its modified versions for different porous structures [22], viscosity is a key parameter that affects both the saturation limit and the wicking rate, and even the slightest increase in viscosity of the penetrating fluid can slow down the rate of wicking to a great extent owing to the increment in the viscous drag. The reduction in flow rate here delays the growth rate of the droplet. The spatiotemporal evolution of the liquid-air interface along with the movement of the contact line during the growth of viscous droplet is shown in Fig. 5(a). The representative snapshots of Figs. 5(A)–5(L) in row (i) (and Supplemental Material, Video 2 [54]) correspond to the generation of a droplet of tween 20 solution, whereas, the snapshots 5(A)–5(L) in row (ii) (and Supplemental Material, Video 3 [54]) show the growth of a hexadecane droplet on a yarn. The red arrows mark the position of tip of the droplet in Fig. 5(a). The movement of the tip for both the liquids clearly suggests the presence of all the three regimes as encountered previously in case of water droplets. However, a one-to-one comparison of the snapshots reveals that the onset of each regime, as well as the transition from one regime to another, is significantly delayed in the physical timescale, as the viscosity of the imbibing fluid is increased even by a marginal amount.

Figure 5(b) shows the time-varying trajectories of the tip z_{tp} and bottom z_{bt} of the droplets generated during the experimental conditions corresponding to Fig. 5(a). The two different colors (magenta and blue) of the corresponding symbols (circle and diamond) signify the two different experimental fluids tween 20 solution (Twn20) and hexadecane (Hexd), respectively. It can be clearly comprehend that even with the slightest increase in the viscosity value, the incipience of each stage of droplet growth is delayed, thereby further delaying the transition from one regime to the other, as claimed previously. For example, in case of tween 20 solution, the end of the "radial growth" stage and transition to the "axial growth" stage takes place approximately at 50 s, whereas for, hexadecane this marks only the beginning of the radial growth stage in physical timescale. The interfacial shape change of the droplet is also expected to follow the delayed transition regimes. Notably, the shape of the droplet in all the experimental conditions follows the Young-Laplace equations as shown in Appendix A.

C. Self-similar contact line and interface profile evolution

A cumulative appraisal of the dynamics of the contact line during the growth of the droplet encompassing all the experimental conditions can be drawn by representing the trajectory in a nondimensional framework of z_{tp} as shown in Fig. 6(a). The nondimensionalization of both z_{tp} and t has been done with the help of the maximum value of the corresponding identities, i.e., $z_{tp}^* = z_{tp}/z_{tp}^{\max}$ and $t^* = t/t_{\text{total}}$, wherein t_{total} is the total time taken for the generation of one drop in each experimental cycle and $z_{tp}^{\max}$ is the maximum value of z_{tp} within that time period t_{total}. It is to note that t_{total} signifies the total time span observed for each experiment calculated from the beginning of the radial growth stage to the final detachment of the droplet from the yarn. This kind of unique nondimensionalization helps in extracting information regarding the rate of evolution of each dependent variable over a unit time span and one-to-one comparison of each relevant quantity in different experimental conditions. Figure 6(a) shows the variation of z_{tp}^* with t^* in a log-log scale for all the experimental conditions studied herein. The presence of three distinct regimes during the droplet growth becomes more evident from Fig. 6(a) wherein all the nondimensional profiles of z_{tp}^* collapsed to a single trajectory, despite starting from different initial instants. This hint toward the presence of self-similarity in the contact line profile evolution in the later stages of the droplet growth period, specifically in "motion" stage, irrespective of the initial conditions. Another important observation from Fig. 6(a) is the presence of two shallow windows for the transition of the contact line dynamics from one regime to the another, which are marked by two differently hashed zones. A qualitative assessment

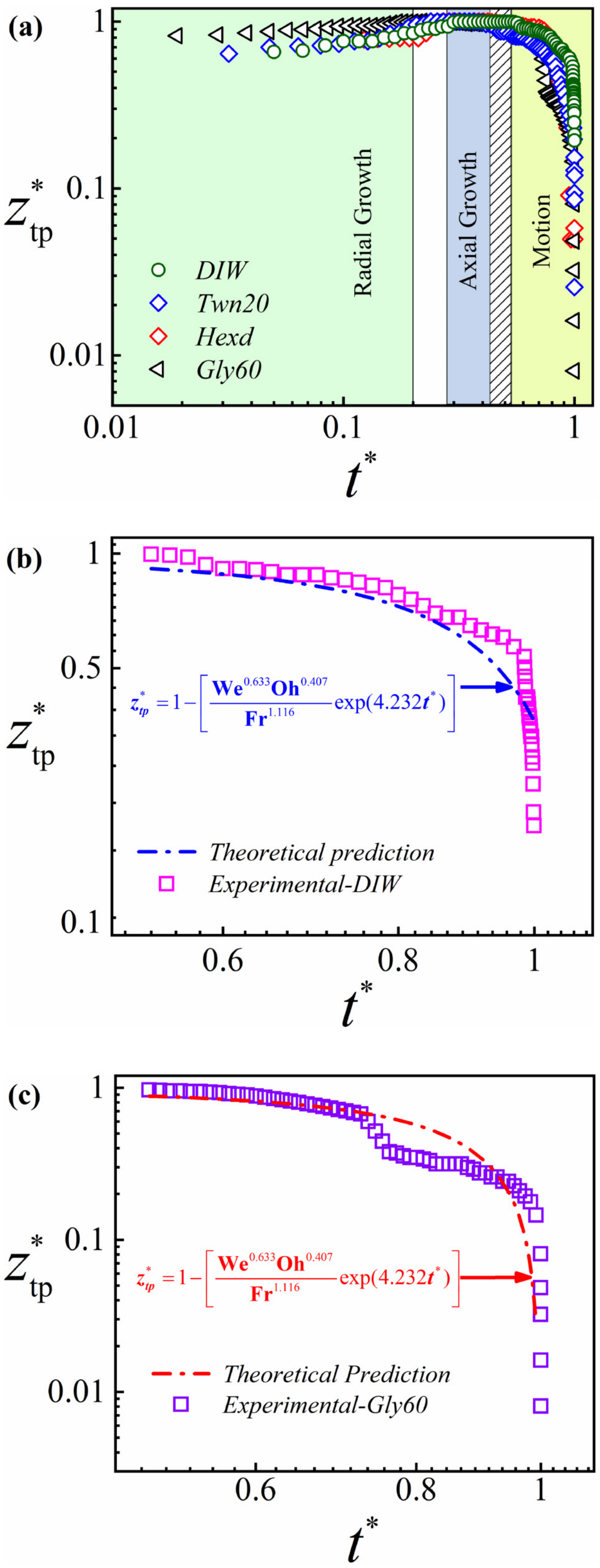

FIG. 6. (a) The variation of the nondimensional tip position z_{tp}^* with nondimensional time t^* is plotted in a log-log scale for all the experimental conditions. The vertical shaded regimes correspond to the transition regimes separating the three stages of drop growth. (b), (c) Compare the experimental data of z_{tp}^* with the derived asymptotic relation (dashed-dotted line) [Eq. (5)] for water (DIW) and 60% glycerol (Gly60) solution, respectively.

of the data reveals that the dynamics of the contact line switches from the radial growth stage to the axial growth one approximately within the first 20%–30% of total time span for the experimental conditions studied herein. The second transition window appears in 45%–55% of the total time taken for droplet growth, where the dynamics transform from the axial growth stage to the "motion" stage.

The self-similarity between the transient dynamics of the contact line during the motion stage can be modeled by considering the competing forces during the period, which are, namely, capillary force, viscous drag, and gravity. The capillary force at the tip can be expressed as [56] $F_c = 2\pi\gamma r_y \cos\theta_c$, whereas the viscous force on the droplet appears as $F_v = -2\pi\eta l_{wt}\frac{v}{\ln\left(\frac{r_d}{r_y}\right)}$ [45,57]. Herein, v, θ_c, and l_{wt} signify the vertical velocity of z_{tp}, contact angle, and wetted length of the yarn, respectively. The viscous drag has been derived after solving the momentum conservation equation in cylindrical coordinates for the droplet, subjected to the boundary conditions of zero vertical velocity (v_z) along the outer surface of the yarn ($r = r_y$) and equal to the velocity of the drop at its interface ($v_z = v$ and $r = r_d$), and deriving the shear-stress term as $\eta\frac{dv_z}{dr}|_{r=r_y} = -\frac{\eta v}{r_y \ln\left(\frac{r_d}{r_y}\right)}$, where $\frac{dv_z}{dr}$ is the velocity gradient along the radial direction (r). The shear stress acts over the surface around the cylindrical yarn $2\pi r_y l_{wt}$, resulting in the viscous friction force F_v during the movement of the droplet. Considering the gravitational force as $F_g = mg$, where m is the instantaneous mass of the liquid drop, the governing equation can be written in the following form:

$$\frac{d(mv)}{dt} = 2\pi\gamma r_y \cos\theta_c \pm 2\pi\eta l_{wt}\frac{v}{\ln\left(\frac{r_d}{r_y}\right)} - mg. \tag{1}$$

The mass of the drop can be expected to increase linearly with time, i.e., $m = \dot{m}(t - t_0)$, where $\dot{m}$ is the mass flux and t_0 is the initial time at the beginning of the drop formation. However, qualitative analysis (refer Sec. III D) of the experimental data clearly shows that the change in the mass of the droplet is negligible in the motion stage, and we can consider the mass to be constant during the period. By introducing the following dimensionless characteristic variables

$$l^*_{wt} = \frac{l_{wt}}{L}, \quad t^* = \frac{t}{\tau}, \quad m^* = \frac{m}{\rho r^3}, \quad v^* = \frac{v}{v_{\text{avg}}} = \frac{v}{\frac{R}{\tau}}, \tag{2}$$

where L and $\tau = t_{\text{total}}$ are the characteristic length and timescale, respectively. Substituting the dimensionless characteristic variables from Eq. (2), Eq. (1) can be converted to the following nondimensional form:

$$\frac{d(m^*v^*)}{dt^*} = \frac{2\pi\,\cos\theta_c}{\text{We}} \pm \frac{2\pi}{\text{Re}\ln\left(\frac{r_d}{r_y}\right)}v^*l^*_{wt} - \frac{1}{\text{Fr}^2}m^*. \tag{3}$$

Here, the Weber number We and Froude number Fr bear the same definition as discussed in Sec. II. The Reynolds number Re signifies the balance between the inertia force and the viscous force and defined as $\text{Re} = \rho v_{\text{avg}}L/\eta$ with v_{avg} being the characteristic velocity scale as seen in Eq. (2). Interestingly, Eq. (3) bears the same form of the governing equation as mentioned in Chang *et al.* [45] for droplet formation in a wettable nozzle. Substituting $\text{Oh} = \frac{\text{We}^{1/2}}{\text{Re}}$ in Eq. (3), we obtain Eq. (4) in terms of the nondimensional numbers considered in this study as

$$\frac{d(m^*v^*)}{dt^*} = \frac{2\pi\,\cos\theta_c}{\text{We}} \pm \frac{2\pi}{\frac{\text{We}^{1/2}}{\text{Oh}}\ln\left(\frac{r_d}{r_y}\right)}v^*l^*_{wt} - \frac{1}{\text{Fr}^2}m^*. \tag{4}$$

Equation (4) shows the important nondimensional groups, namely, We, Fr, and Oh, necessary for determining the scaling law for z^*_{tp} with respect to time t^* during the downward movement of the drop. A regression analysis (explained in Appendix B) of all the experimental data sets suggests the following correlation between z^*_{tp} and t^*:

$$z^*_{tp} = 1 - \left(\frac{\text{We}^{0.633}\text{Oh}^{0.407}}{\text{Fr}^{1.116}}\exp(4.232t^*)\right). \tag{5}$$

An account of the exponents of the nondimensional groups of Eq. (5) clearly reflects that the gravity force dominates the transient dynamics of the contact line z_{tp} in this third regime of droplet growth. Although surface tension tries to resist the droplet motion, its effect appears to be weaker than the weight of the droplet as soon as it starts descending along the yarn. The asymptotic relation between z^*_{tp} and t^* gives a good agreement with the experimental data as seen in Figs. 6(b) and 6(c), which shows the transient evolution of z^*_{tp} in the third regime in case of water and 60% glycerol solution, respectively. The scaling law reported above [Eq. (5)] has a good resemblance with the asymptotic relation proposed by Chang *et al.* [45]. However, the latter has shown a parabolic fit of the position of the contact line of the droplet while it descends along a wettable nozzle, whereas we observe an exponential decrease of z^*_{tp} in this study.

Furthermore, the spatiotemporal evolution of the interface of the droplet during its growth can be well understood by plotting the variation of the nondimensional radius r^*_d with time t^* as shown in Fig. 7(a). Herein, the physical timescale has been nondimensionalized as discussed previously, whereas the maximum values of the droplet radius $r^{\max}_d$ over the considered time span t_{total} has been used as the scale for nondimensionalization of the radius. Figure 7(a) clearly shows that, irrespective of the experimental conditions, all the profiles of r^*_d follow a similar kind of asymptotic trajectory during the growth period. However, the vertical shift of the profiles can be attributed to the variations in their thermophysical properties. Also, the initially separated profiles converge beyond a specific time instant, as seen in Fig. 7(a). A quantitative assessment of the experimental data reveals that the profile converges approximately at 55% of their total time period, which is also, coincidentally, the transition point of the contact line dynamics from the axial growth stage to the motion stage. Until this transition point, the radius of the droplet grows to nearly 90%–95% of its final value. Hence, the third stage involves very little change in the radius as well as the droplet volume, which also strengthens our previous claim that the mass of the droplet remains nearly constant during that period.

Here, we wish to find a scaling law defining the self-similar profiles of the interfaces, specifically r^*_d observed during the first two stages of growth of the droplet with the help of previously mentioned nondimensional groups: We, Oh, and Fr. The regression analysis (refer to Appendix B) of the experimental data of r^*_d suggest the following asymptotic

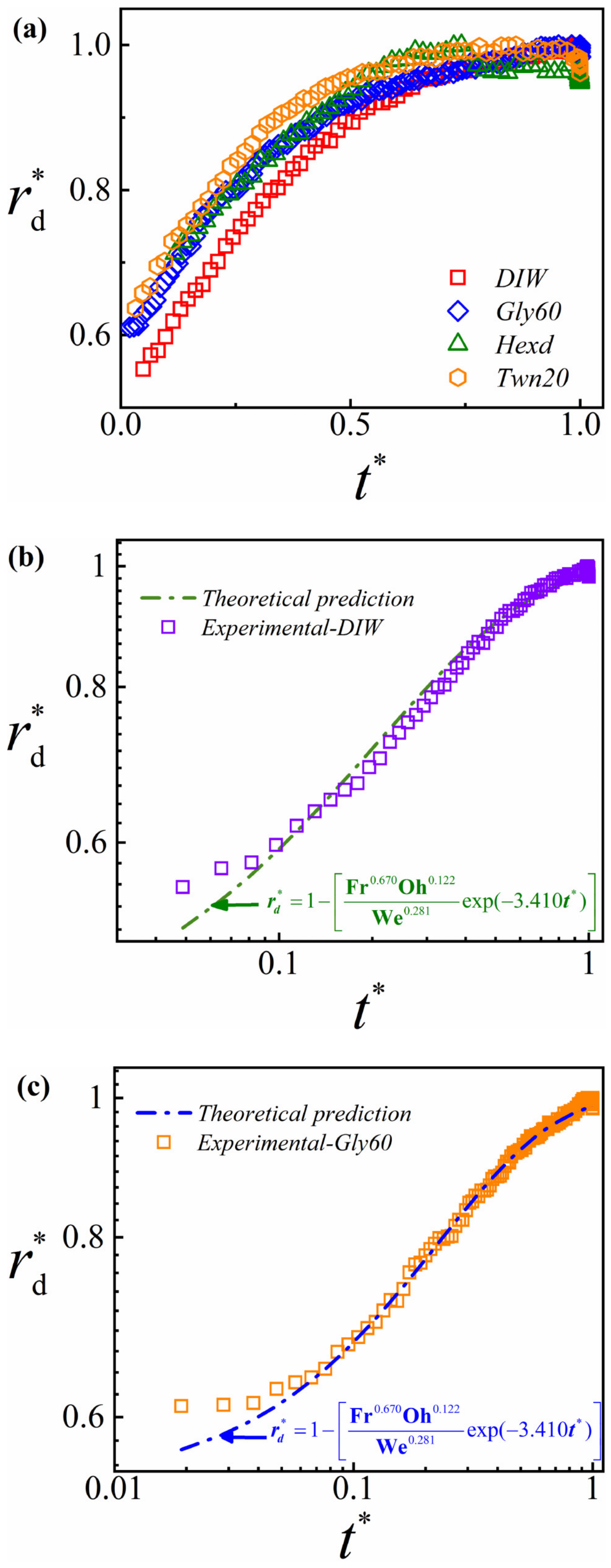

FIG. 7. (a) Linear plot of variation of nondimensional radius r_d^* with nondimensional time t^* of a continuously growing droplet at different experimental conditions corresponding to Table II. Logarithmic plots of r_d^* with t^* exhibit the good agreement between the derived scaling law (dashed-dotted line) [Eq. (6)] and the experimental data for (b) water and (c) 60% glycerol solution. respectively.

scaling law:

$$r_d^* = 1 - \left(\frac{\mathrm{Fr}^{0.670}\mathrm{Oh}^{0.122}}{\mathrm{We}^{0.281}}\exp(-3.410t^*)\right). \tag{6}$$

The inversely proportional relation between the Weber number We and r_d^* in Eq. (6) signifies the logical trend of a fluid with higher surface tension trying to hold a droplet of greater radius. The asymptotic relation of Eq. (6) also suggests that the capillary force dominates the gravity force during the first stages of growth and this results in the upward movement of the tip, as well as higher radial expansion in the initial period, as discussed previously. As per Eq. (6), the rate of change of the droplet radius will be more in the initial periods which eventually slows down and, finally, the radius of the droplet will remain nearly constant, which coincides with our observation in Fig. 7(a). The good agreement between the experimentally measured data and theoretical prediction can be seen in Figs. 7(b) and 7(c) plotted for two fluids, water and 60% glycerol solution, respectively. It is to note that the scaling relation [Eq. (6)] in this study differs greatly from the scaling law $D_d^* = (4 + 6t^*)^{(1/3)}$ obtained in case of generation of a droplet from an orifice under constant flow condition [38]. The latter takes care of the growth of a spherical droplet constantly adhering to a nozzle exit, in contrast to this study where the droplet undergoes changes from barrel to pear shape, and is never spherical. Equation (6) has been derived in the purview of this difference in basic assumption, considering the contributions of the thermophysical properties of the experimental fluids.

D. Estimation of critical volume required for sliding

We now wish to find the critical volume V_{sl}^{cr} of the droplet which is nothing but the maximum volume attained by the droplet prior to the beginning of downward sliding from its maximum position and has a direct effect on the final volume of the detached droplet. The instant of occurrence of V_{sl}^{cr} is the point of transition between the second and the third stages. As estimated previously, r_d attains nearly 90%–95% of its final radius, whereas l_d reaches nearly 80% of its total length until the end of the second stage. Approximating the droplet shape with an annular cylinder, i.e., $V_{sl}^{cr} \sim ZR^2 \sim l_d^{cr}(r_d^{cr})^2$, it can be estimated that the droplet volume nearly attains 70%–80% of its total volume (i.e., volume of the detached primary droplet) just before initiating the downward motion in each experimental condition. Here, r_d^{cr} and l_d^{cr} represent the critical radius and the length of the droplet at the instant of measurement of V_{sl}^{cr}, respectively.

By considering the delicate balance between the driving and the resisting forces, V_{sl}^{cr} can be estimated theoretically. Along with the driving force F_g and the resisting force F_c, mentioned in Sec. III C, the capillary force due to the presence of a liquid film along the yarn F_{fc} has also been considered as another resisting force while estimating V_{sl}^{cr}. However, the viscous drag F_v has not been considered herein, due to the negligible velocity of the interface at the onset of sliding motion. The transition from the axial growth stage to the motion stage occurs once F_g just overcomes the static friction offered by F_c and F_{fc} for a droplet of volume V_{sl}^{cr}. Notably, both the resisting forces are larger when the surface tension is

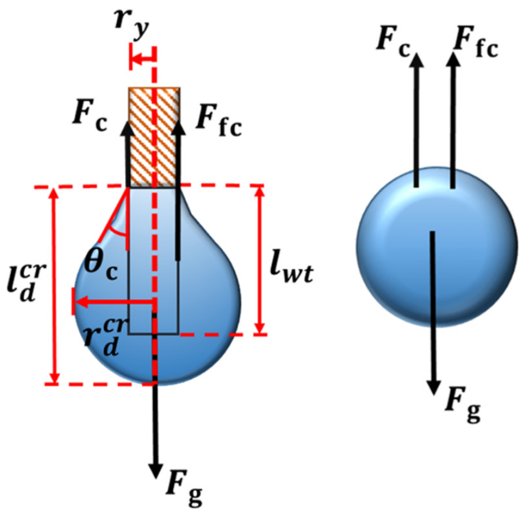

FIG. 8. Force balance in case of a drop continuously growing on a yarn just prior to the initiation of sliding motion. The different geometrical parameters of the drop considered in the force balance are shown with the help of dimensional arrows. F_g is the gravitational pull experienced by the droplet due to its own weight, F_c is the capillary force along the contact line, and F_{fc} is the capillary force due to the liquid film acting along the wetting length l_{wt}.

higher. The resisting force due to the liquid film also depends upon the droplet wetting length l_{wt} and becomes large with higher film thickness.

The discussed force balance, shown schematically in Fig. 8, can be written as

$$F_g = F_c + F_{fc}. \tag{7}$$

The gravitational force experienced by the drop can be rewritten as $F_g = \rho g V_{sl}^{cr} = \frac{4\pi}{3}(r_d^{cr})^3 \rho g$ assuming the droplet to be spherical in shape for simplifying the calculations. The capillary force due to the liquid film [58] can be written as $F_{fc} = \gamma l_{wt}$, where the wetting length is $l_{wt} = 2\zeta_l^{sl} r_d^{cr}$, with ζ_l^{sl} as the fitting parameter that takes into account the deviation of the droplet shape from the spherical shape. The final form of Eq. (7) can be found as follows:

$$\frac{4\pi}{3}\left(r_d^{cr}\right)^3 \rho g - 2\gamma \zeta_l^{sl} r_d^{cr} - 2\pi\gamma r_y \cos\theta_c = 0. \tag{8}$$

The cubic equation (8) with positive polynomial discriminant has the single real solution as follows:

$$r_d^{cr} = \sqrt[3]{\frac{3\lambda^2 r_y \cos\theta_c}{4} + \sqrt{\left(\frac{3\lambda^2 r_y \cos\theta_c}{4}\right)^2 - \left(\frac{\zeta_l^{sl}\lambda^2}{2\pi}\right)^3}} + \sqrt[3]{\frac{3\lambda^2 r_y \cos\theta_c}{4} - \sqrt{\left(\frac{3\lambda^2 r_y \cos\theta_c}{4}\right)^2 - \left(\frac{\zeta_l^{sl}\lambda^2}{2\pi}\right)^3}}, \tag{9}$$

where $\lambda = \sqrt{\gamma/\rho g}$ is the capillary length. Based on the value of the critical radius r_d^{cr} obtained from Eq. (9), the theoretical critical volume $V_{sl}^{cr} = \frac{4\pi}{3}\zeta_V^{sl}(r_d^{cr})^3$ can be calculated where ζ_V^{sl} is a geometric prefactor taking into account the deviation of V_{sl}^{cr} from its actual drop volume [58]. A critical comparison of the experimental data with the theoretical volume data shows that irrespective of the different thermophysical properties of the experimental fluids, the value of ζ_V^{sl} is fixed at $\zeta_V^{sl} = 0.7 \pm 0.15$. Also, the fitting parameter ζ_l^{sl} accounting for the wetting length comes out to be close to each other for different experimental conditions and found to be in the range of $\zeta_l^{sl} = 0.57 \pm 0.13$. The consideration of the geometric prefactor and fitting parameter in this study nullifies the deviation in the V_{sl}^{cr}, appearing as a result of considering the droplet to be spherical in shape.

E. Dynamics of droplet detachment: Static pinch-off

The dynamics of the growth stage comes to an end as soon as the tip reaches the end of the yarn and the detachment phase of the droplet begins (refer to Supplemental Material, Videos 4, 5, and 6 [54]). Owing to the very low flow rate of the penetrating fluid through the capillary network of the yarn, i.e., extremely small We conditions (of the order of 10^{-9}), the dynamics of detachment adheres to the laws of "static pinch-off" regime, wherein, the subsequent outcomes such as the size of the detached primary droplet (V_d^{pin}), the volume of the remnant fluid after breakup, etc., solely depend on the competition between the gravitational force and the capillary force ($2\pi\gamma r_y$) [59]. As reported by Harkins and Browns [59], in the static-pinch-off regime, the detached primary droplet volume V_d^{pin} can be determined as follows:

$$V_d^{\text{pin}} = \zeta_V^{\text{pin}}\left(\frac{2\pi\gamma r_y}{g\rho}\right), \tag{10}$$

where the Harkins-Brown compensation factor ζ_V^{pin} is defined as the ratio of the volume of the primary droplet detached from the nozzle V_d^{pin} to the maximum volume of the liquid balanced by the capillary force at the nozzle exit [the term within parentheses in the right-hand side of Eq. (10)]. Conventionally, expressed as $\zeta_V^{\text{pin}} = f(r/V_d^{\text{pin}\,1/3})$, the compensation factor assumes different forms and numerical values depending upon the nozzle and the liquid pair and thereby ensuring that post detachment, a fraction of the total volume remains attached to the nozzle exit.

Figure 9 shows the experimentally measured drop volumes for four different liquids listed in Table I, which are being designated by the corresponding We as listed in Table II. The volume of the released drop decreases sharply with a decrease in We as seen in Fig. 9, which demonstrates the fact that higher surface tension force is capable of holding a larger drop volume prior to pinch-off. A suitable fitting method shows that $\zeta_V^{\text{pin}} = 0.67$ allows us to adhere to the lowest limit of experimentally measured volumes for the entire range of We explored in this study, as shown by the lowermost solid line (with symbols) in Fig. 9. The uppermost curve corresponds to the maximum volume of the hanging drop that can be supported by the yarn, i.e., $\zeta_V^{\text{pin}} = 1$, which is nothing but the weight of the "ideal drop" as determined by Tates law [60]. In the absence of a unique value of ζ_V^{pin} in literature, the present approach of representing the measured data via a range of parameters (0.67–1.0) seems to be the only viable option and hence has been adopted in the present analyses. If the surface

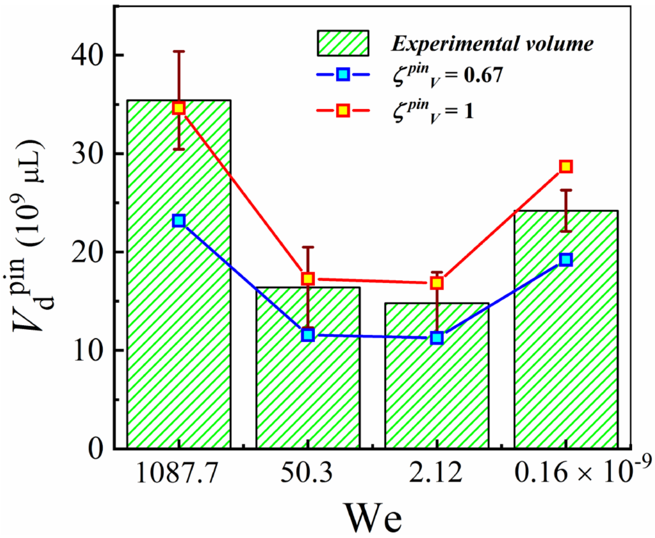

FIG. 9. Comparison between the experimentally measured primary drop volume and theoretical law from Harkins and Browns [59].

tension of the fluid is known beforehand, the reported values of the compensation factor may help in predicting the final volume of a droplet detached from a yarn.

IV. CONCLUSIONS

This study reports a qualitative assessment of the dynamics of the generation and detachment of a droplet from a yarn under different experimental conditions. A simple drop generation facility has been engendered by the continuous capillary flow within the yarn, which facilitates a comparison of the present system with the existing methods of drop formation from a capillary tube. The study focuses on the temporal evolution of the three-phase contact line, as well as the interface of a growing droplet. Here, the contact line follows a distinct repetitive pattern, characterized by sequential radial and axial growth, which is contrary to the existing drop generation systems, where the contact line constantly adheres to the outer wall of the capillary tube (or nozzle). Depending on the relative positioning of the contact line, the complete growth cycle of a Newtonian droplet on a yarn can be divided into three distinct regimes, namely, "radial growth," "axial growth," and "motion." During the former, the radius of the drop expands rapidly with a relatively moderate rate of increase in the length. The "tip" of the drop moves upward in this stage due to the dominance of the surface tension force over the gravity force, while the "bottom" remains fixed around the free end of the yarn. A relatively higher increment in the drop length and slower expansion of radius are the characteristics of the second stage, with the "tip" adhering to its maximum position over the entire span and the "bottom" point continuously moving away from the datum. The second stage comes to completion with the droplet reaching a critical volume, enabling it to overcome the resisting forces preventing it from sliding downward. Interestingly, the critical volume required for the drop to initiate sliding has been found to be 70%–80% of the final drop volume after pinch-off, a value deduced from the quantitative analysis of the experimental images, as well as theoretically. The contact line dynamics during the "motion" stage is found to be self-similar irrespective of the initial experimental conditions, which can be described by an asymptotic scaling relation based on the combined effect of driving and resisting forces. The scaling relation suggests that gravity force dominates upon the capillary forces during the third stage. Another asymptotic relation has been proposed for the evolution of the radius of the droplet during its growth. The derived relations suggest that the surface tension force dominates the growth rate of the droplet during the initial two stages, which in turn controls the final droplet volume. By using a number of fluids, spanning across a wide range of viscosity, we found that for the macroscale contact line dynamics occurring over a physical timescale, viscosity plays the role of rate limiter. Furthermore, the very low flow rates during the experiments directed the dynamics of drop formation in the "static-pinch-off" regime.

The findings of this study may stimulate further investigations on the transient dynamics of a droplet generating from a yarn with different chemical and physical textures. Also, more experiments with liquids having wider ranges of the relevant properties including nonwetting fluids can be performed to extend the validity of the proposed asymptotic relations. Moreover, careful numerical simulations may shed light in understanding the dynamics of drop formation in naturally observed as well as synthetic hierarchical porous structures.

ACKNOWLEDGMENTS

The authors would like to express sincere gratitude to Dr. D. Bandopadhyay of the Chemical Engineering Department, IIT Guwahati, for allowing the use of the state-of-the-art experimental facility of his laboratory throughout the experimental period. Also, we would like to thank Dr. G. Natarajan (Department of Mechanical Engineering, IIT Palakkad) and Dr. A. K. Singh (Centre for Nanotechnology, IIT Guwahati) for many useful discussions.

APPENDIX A: ESTIMATION OF THE DROP SHAPE

In this study, although drop formation has been engendered by a flow field with very low flow rate, the well-established Young-Laplace equation could predict the shape of the drop at all the three stages mentioned previously. The differential equations that define the axisymmetric shape of a growing drop attached to the yarn are as follows;

$$\frac{dr}{ds} = \cos(\theta), \tag{A1}$$

$$\frac{dz}{ds} = \sin(\theta), \tag{A2}$$

$$\frac{d\theta}{ds} = 2\kappa_0 - \left(\frac{1}{\lambda^2}\right)z - \frac{\sin(\theta)}{r}, \tag{A3}$$

with the initial conditions prescribed as $r(0) = 0$; $z(0) = z_{\min}$ and $\theta(0) = 0$.

As shown in Fig. 10(a), s represents the arc length, κ_0 is the curvature at the apex, $z_{\min}$ is the position of the apex, and λ is the capillary length as defined previously. The droplet

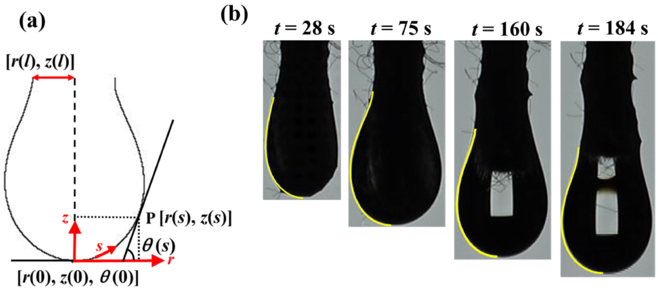

FIG. 10. (a) Schematic of an axisymmetric drop attached to a capillary with all the spatial and angular variables defining the shape at each instant. (b) Comparison between the numerically obtained droplet shape (yellow curve) with the shape obtained experimentally by fitting the former upon the latter. The axisymmetric equations are able to describe the shape well as the yellow curve fits completely the experimental shapes. The experimental conditions encountered are $Q^{\mathrm{Twn20}} = 8.68 \times 10^{-11}$ m^3/s, We $= 5.03 \times 10^{-8}$, Oh $= 0.0063$, and Fr $= 5.73 \times 10^{-4}$.

shapes obtained after solving Eqs. (A1)–(A3) numerically when fitted over the experimentally generated droplet shapes show a good match as shown in Fig. 10(b), wherein the yellow curve is the shape of the interface obtained numerically. Figure 10(b) corresponds to the different stages of growth of a drop of tween 20 solution from a yarn with experimental conditions $Q^{\mathrm{Twn20}} = 8.68 \times 10^{-11}$ m^3/s, We $= 5.03 \times 10^{-8}$, Oh $= 0.0063$, and Fr $= 5.73 \times 10^{-4}$. Also, as ascribed in Chang *et al.* [45] the contact angle has not been considered as boundary conditions due to the prevalence of contact angle hysteresis between the advancing and receding contact angle while moving along the yarn. Further, the good agreement between the experimental data and theoretical prediction also confirms the universality of the Young-Laplace axisymmetric equations describing the interfacial shape change of a drop growing in a yarn.

APPENDIX B: DETAILS OF REGRESSION ANALYSIS

By having a closer look in Fig. 6(a), the relation between z^*_{tp} and t^* in the "motion stage" can be defined as below:

$$z^*_{tp} = 1 - [\mathrm{We}^a \mathrm{Oh}^b \mathrm{Fr}^c \exp(dt^*)], \tag{B1}$$

where, a, b, c, and d are experimentally fitted constants. The regression analysis is carried out using the Levenberg-Marquardt algorithm, which is being popularly used in many industrial optimization processes including the pendant drop shape optimization routines [61]. This nonlinear least-square optimization algorithm combines the speed and the accuracy of both Gauss-Newton optimization and the steepest descent method and optimizes the iterations by considering the minimization of the sum of the squared residuals between each experimental data point and corresponding theoretical data points [62,63]. The parametric convergence criteria have been set as $1E^{-8}$ for the present regression analysis, which resulted in 38 iterations for evaluation of the constants of Eq. (B1). The regression analysis of the experimental data resulted in the following equation:

$$z^*_{tp} = 1 - \left(\frac{\mathrm{We}^{0.633} \mathrm{Oh}^{0.407}}{\mathrm{Fr}^{1.116}} \exp(4.232 t^*) \right). \tag{B2}$$

The standard values of the fitted coefficients in Eq. (B2) are $a = 0.633 \pm .031$, $b = 0.407 \pm .015$, $c = -1.116 \pm .064$, and $d = 4.323 \pm 0.109$. The corresponding values of the regression coefficient R^2 and the mean squared error (MSE) are found out to be 0.930 and 0.009, respectively.

A similar type of regression analysis has been carried out for obtaining the scaling relation (6) between r^*_d and t^*. The values and range of the fitted coefficients a, b, c, and d in the case of Eq. (6) are found out to be $0.281 \pm .022$, $0.122 \pm .008$, $0.670 \pm .048$, and -3.410 ± 0.045, respectively. The value of the regression coefficient R^2 is 0.963, whereas the mean squared error has been found out as 0.0001.

---

[1] E. W. Washburn, Phys. Rev. **17**, 273 (1921).

[2] L. A. Richards, Physics **1**, 318 (1931).

[3] N. R. S. Hollies, M. M. Kaessinger, and H. Bogaty, Text. Res. J. **26**, 829 (1956).

[4] S. R. Brown, J. Geophys. Res. **92**, 1337 (1987).

[5] D. Danino and A. Marmur, J. Colloid Interface Sci. **166**, 245 (1994).

[6] M. Conrath, P. J. Canfield, P. M. Bronowicki, M. E. Dreyer, M. M. Weislogel, and A. Grah, Phys. Rev. E **88**, 063009 (2013).

[7] C.-C. Tsai, Y. Gu, and K. G. Kornev, Colloids Surf. A **459**, 22 (2014).

[8] Y.-L. Hsieh, Text. Res. J. **65**, 299 (1995).

[9] K. P. M. Tang, K. H. Chau, C. W. Kan, and J. T. Fan, Sci. Rep. **5**, 17012 (2015).

[10] W. Benjamin and S. Beckwith, *Resin Transfer Moulding*, SAMPE Monograph 3 (SAMPE, Covina, CA, 1999).

[11] M. Reches, K. A. Mirica, R. Dasgupta, M. D. Dickey, M. J. Butte, and G. M. Whitesides, ACS Appl. Mater. Interfaces **2**, 1722 (2010).

[12] R. Safavieh, G. Z. Zhou, and D. Juncker, Lab Chip **11**, 2618 (2011).

[13] K. Cherenack and L. van Pieterson, J. Appl. Phys. **112**, 091301 (2012).

[14] B. White, Can. Soc. Forensic Sci. J. **19**, 3 (1986).

[15] X. Li, J. Li, and S. Michielsen, Forensic Sci. Int. **276**, 41 (2017).

[16] L. Fourt, A. M. Sookne, D. Frishman, and M. Harris, Text. Res. J. **21**, 26 (1951).

[17] N. Pan and P. Gibson, *Thermal and Moisture Transport in Fibrous Materials* (CRC Press, Boca Raton, FL, 2006).

[18] N. R. S. Hollies, M. M. Kaessinger, B. S. Watson, and H. Bogaty, Text. Res. J. **27**, 8 (1957).

[19] E. Kissa, Text. Res. J. **66**, 660 (1996).

[20] A. Perwuelz, P. Mondon, and C. Caze, Text. Res. J. **70**, 333 (2000).

[21] T. Liu, K.-f. Choi, and Y. Li, J. Colloid Interface Sci. **318**, 134 (2008).

[22] S. Beyhaghi, S. Geoffroy, M. Prat, and K. M. Pillai, AIChE J. **60**, 1930 (2014).

[23] T. Shield, D. Bogy, and F. Talke, IBM J. Res. Dev. **31**, 96 (1987).

[24] O. A. Basaran, H. Gao, and P. P. Bhat, Annu. Rev. Fluid Mech. **45**, 85 (2013).

[25] W. A. Sirignano, *Fluid Dynamics and Transport of Droplets and Sprays*, 2nd ed. (Cambridge University Press, Cambridge, 2010).
[26] N. Ashgriz, *Handbook of Atomization and Sprays: Theory and Applications* (Springer, New York, 2011).
[27] R. F. Service, Science **282**, 396 (1998).
[28] P. Umbanhowar, V. Prasad, and D. A. Weitz, Langmuir **16**, 347 (2000).
[29] T. Thorsen, R. W. Roberts, F. H. Arnold, and S. R. Quake, Phys. Rev. Lett. **86**, 4163 (2001).
[30] X. Zhang and O. A. Basaran, Phys. Fluids **7**, 1184 (1995).
[31] C. Clanet and J. C. Lasheras, J. Fluid Mech. **383**, 307 (1999).
[32] A. D'Innocenzo, F. Paladini, and L. Renna, Phys. Rev. E **65**, 056208 (2002).
[33] B. Ambravaneswaran, H. J. Subramani, S. D. Phillips, and O. A. Basaran, Phys. Rev. Lett. **93**, 034501 (2004).
[34] R. Schulkes, J. Fluid Mech. **278**, 83 (1994).
[35] D. Zhang and H. Stone, Phys. Fluids **9**, 2234 (1997).
[36] A. U. Chen, P. K. Notz, and O. A. Basaran, Phys. Rev. Lett. **88**, 174501 (2002).
[37] J. R. Castrejón-Pita, A. A. Castrejón-Pita, S. S. Thete, K. Sambath, I. M. Hutchings, J. Hinch, J. R. Lister, and O. A. Basaran, Proc. Natl. Acad. Sci. USA **112**, 4582 (2015).
[38] M. P. Borthakur, G. Biswas, and D. Bandyopadhyay, Phys. Rev. E **96**, 013115 (2017).
[39] M. Rubio-Rubio, P. Taconet, and A. Sevilla, Int. J. Multiphase Flow **104**, 206 (2018).
[40] H. Dong, W. W. Carr, and J. F. Morris, Rev. Sci. Instrum. **77**, 085101 (2006).
[41] M. Versluis, Exp. Fluids **54**, 1458 (2013).
[42] E. Hauser, H. Edgerton, B. Holt, and J. Cox Jr, J. Phys. Chem. A **40**, 973 (1936).
[43] D. H. Peregrine, G. Shoker, and A. Symon, J. Fluid Mech. **212**, 25 (1990).
[44] P. K. Notz, A. U. Chen, and O. A. Basaran, Phys. Fluids **13**, 549 (2001).
[45] B. Chang, G. Nave, and S. Jung, Commun. Nonlinear Sci. Numer. Simul. **17**, 2045 (2012).
[46] A. Taur, P. Doshi, and H. K. Yeoh, Eur. J. Mech. B Fluids **51**, 8 (2015).
[47] M. Z. Miskin and H. M. Jaeger, Proc. Natl. Acad. Sci. USA, **109**, 4389 (2012).
[48] B. Zhmud, F. Tiberg, and K. Hallstensson, J. Colloid Interf. Sci. **228**, 263 (2000).
[49] Q. Li, J. Wang, and C. Hurren, J. Nat. Fibers **14**, 400 (2017).
[50] P. Randive, A. Dalal, K. C. Sahu, G. Biswas, and P. P. Mukherjee, Phys. Rev. E. **91**, 053006 (2015).
[51] Y. Wu and S. Gao, *Advances in Future Computer and Control Systems* (Springer, Berlin, 2012), pp. 477–481.
[52] J. Castrejón-Pita, S. Willis, and A. Castrejón-Pita, Rev. Sci. Instrum. **86**, 115101 (2015).
[53] C. A. Schneider, W. S. Rasband, and K. W. Eliceiri, Nat. Methods **9**, 671 (2012).
[54] See Supplemental Material at http://link.aps.org/supplemental/10.1103/PhysRevE.100.013106 for experimental videos. Video 1, 2 and 3 show the growth dynamics of droplets of DI-water, Tween 20 solution and hexadecane respectively. High-speed videos 4, 5, and 6 show the detachment dynamics of droplets of DI-water, Tween 20 solution and hexadecane, respectively.
[55] A. Patnaik, R. S. Rengasamy, V. K. Kothari, and A. Ghosh, Textile Progress **38**, 1 (2006).
[56] É. Lorenceau, C. Clanet, and D. Quéré, J. Colloid Interface Sci. **279**, 192 (2004).
[57] A. L. Yarin, W. Liu, and D. H. Reneker, J. Appl. Phys. **91**, 4751 (2002).
[58] F. Weyer, A. Duchesne, and N. Vandewalle, Sci. Rep. **7**, 13309 (2017).
[59] W. D. Harkins and F. Brown, J. Am. Chem. Soc. **41**, 499 (1919).
[60] T. Tate, Philos. Mag. **27**, 176 (1864).
[61] O. Del Rio and A. W. Neumann, J. Colloid Interface Sci. **196**, 136 (1997).
[62] K. Levenberg, Q. Appl. Math. **2**, 164 (1944).
[63] D. W. Marquardt, SIAM J. Appl. Math. **11**, 431 (1963).